

Xiaofeng Liu · Joseph Katz

# Instantaneous pressure and material acceleration measurements using a four-exposure PIV system

Received: 19 November 2005 / Revised: 29 March 2006 / Accepted: 10 April 2006 / Published online: 3 May 2006  
© Springer-Verlag 2006

**Abstract** This paper describes a non-intrusive technique for measuring the instantaneous spatial pressure distribution over a sample area in a flow field. A four-exposure PIV system is used for measuring the distribution of material acceleration by comparing the velocity of the same group of particles at different times and then integrating it to obtain the pressure distribution. Exposing both cameras to the same particle field at the same time and cross-correlating the images enables precision matching of the two fields of view. **Application of local image deformation correction to velocity vectors measured by the two cameras reduces the error due to relative misalignment and image distortion to about 0.01 pixels in synthetic images.** An omni-directional virtual boundary integration scheme is introduced to integrate the acceleration while minimizing the effect of the local random errors in acceleration. Further improvements are achieved by iterations to correct the pressure along the boundary. Typically 3–5 iterations are sufficient for reducing the incremental mean pressure change in each iteration to less than 0.1% of the dynamic pressure. Validation tests of the principles of the technique using synthetic images of rotating and stagnation point flows show that the standard deviation of the measured pressure from the exact value is about 1.0%. This system is used to measure the instantaneous pressure and acceleration distributions of a 2D cavity turbulent flow field and sample results are presented.

## 1 Introduction

Knowledge of the pressure distribution in a flow field is a primary concern in many engineering applications.

Pressure is the dominant contributor to the lift and form drag for a body moving in fluid. Wall pressure fluctuations are responsible for excitation of structures, leading to flow-induced vibrations and noise (Blake 1986). In turbulence research, the velocity–pressure gradient tensor in the Reynolds stress transport equation, which is typically decomposed into the pressure diffusion and the pressure-strain tensors, is a key unresolved parameter in the modeling of turbulence (Pope 2000; Girimaji 2000). However, due to lack of experimental techniques for simultaneous measurements of pressure and velocity gradients simultaneously, **the velocity–pressure gradient tensor has never been measured directly.** Available experimental data on pressure diffusion has been inferred experimentally in simple geometries from a balance of the other terms in the turbulence kinetic energy transport equations (Gutmark and Wygnanski 1976; Wygnanski and Fiedler 1969; Liu and Thomas 2004). The only source of reliable information is direct numerical simulation (DNS) data, which are also limited to simple geometries and low Reynolds numbers.

Pressure is also of fundamental importance for understanding and modeling cavitation. It is well established that cavitation inception occurs when small bubbles or nuclei in liquid grow explosively due to exposure to low pressure (Brennen 1995; Arndt 2002). However, due to lack of experimental capability, we have very little data on the instantaneous pressure distributions away from boundaries, e.g., in turbulent free shear layers and within tip vortices. To date the only available techniques for pressure measurement away from boundaries are based on Pitot-tube type of probes, such as five hole and seven hole probes. However, these probes are intrusive, not suitable for dynamic measurement due to a limited frequency response, and can only perform point measurements. Although limited instantaneous pressure measurements were performed in the past using microscopic bubbles as pressure sensors (Ooi and Acosta 1983; O'Hern 1990; Ran and Katz 1994), they were not performed simultaneously with velocity

X. Liu · J. Katz (✉)  
Department of Mechanical Engineering,  
Johns Hopkins University, Baltimore, MD 21218, USA  
Tel.: +1-410-5165393  
Fax: +1-410-5164316  
E-mail: katz@jhu.edu  
URL: <http://pegasus.me.jhu.edu/~lefd>

measurements and, more importantly, provided very limited data points. To date even with the detailed velocity measurements provided by PIV, we still do not have direct experimental data on the local instantaneous pressure causing cavitation inception in high Reynolds number flows. In flows involving large coherent structures, we have to infer the pressure distribution using assumed simplified relationships between velocity and pressure, e.g., a Rankine vortex, which at best provides some qualitative insight.

This lack of adequate capability to determine the instantaneous spatial pressure distribution and the need for experimental data provide the motivation for the present on-going effort. We have developed a system that is capable of measuring the instantaneous pressure distribution in a non-intrusive manner based on particle image velocimetry (PIV) technology (Liu and Katz 2003, 2004). This system utilizes four-exposure PIV to measure the distribution of material acceleration and then integrates it to obtain the pressure. This approach provides the distributions of instantaneous pressure, material acceleration and velocity distributions simultaneously.

Acceleration has been studied both numerically and experimentally before. The objectives of most of previous works have been either to provide data for Lagrangian stochastic turbulence models (Yeung 2001, 2002; Vedula and Yeung 1999; Voth et al. 1998; La Porta et al. 2001; Ott and Mann 2000) or to develop techniques for either Lagrangian (material) or Eulerian (local) acceleration measurements (Jakobsen et al. 1997; Dong et al. 2001; Christensen and Adrian 2002; Jensen et al. 2001, 2003; Jensen and Pedersen 2004; Chang and Liu 1998; Chang et al. 1999; Sridhar and Katz 1995). Voth et al. (1998) and La Porta et al. (2001) tracked and calculated the acceleration of individual particles. Dong et al. (2001) obtained 2D Eulerian acceleration distributions using one CCD camera by combining cross-correlations and auto-correlations on two successive, doubly exposed frames. The two instantaneous velocity fields, each obtained from the auto-correlation analysis, were used for computing the acceleration. Chang et al. (1999) proposed a triple-exposure particle tracking method using one camera recording two frames with the first frame containing two exposures and the second frame a single exposure. Particle tracking enables the measurement of the material acceleration. They used this method to measure the acceleration with breaking waves (Chang and Liu 1998). Sridhar and Katz (1995) used triple-exposure images to simultaneously measure the velocity and material acceleration of microscopic bubbles and the fluid surrounding them.

As for the measurement techniques involving two or more cameras, Ott and Mann (2000) used four synchronized CCD cameras to track the trajectories of seed particle pairs and investigated their diffusion characteristics in a turbulent flow generated by two oscillating grids. Jakobsen et al. (1997) utilized a specially designed

four-CCD camera system to obtain the acceleration field near the wall of a surface wave flume based on PIV technology. They validated their acceleration measurement by integrating the averaged acceleration and then comparing it to the mean pressure difference between two wall pressure taps. Christensen and Adrian (2002) measured the instantaneous Eulerian acceleration field of a boundary layer flow using two CCD cameras with cross-polarized laser beams as light sources. They calculated the so-called velocity bulk-convective-derivative field and concluded that the dominant vortical structures remained almost frozen in time. Jensen et al. (2001) measured the Eulerian acceleration in periodic waves using two cameras placed side-by-side to view the same region of the flow. With the same extended PIV setup, Jensen et al. (2003) further proposed a pseudo-tracing technique to measure the material acceleration of wave run-up over a steep beach by tracing imaginary fluid particles between two consecutive velocity fields. In a recent paper on optimization of acceleration measurements, Jensen and Pedersen (2004) compared two methods for extracting material accelerations based on two camera PIV measurements. They concluded that the linear regression of the velocity gradients for the convective acceleration term estimate is more sensitive to random errors in velocity fields while in contrast, the pseudo-tracing approach is more favorable for the wave flow.

The practice of integrating Navier–Stokes equation to obtain pressure along control surfaces can also be found in literature. For example, to obtain the instantaneous force on an oscillating cylinder, Unal et al. (1997) implemented a momentum-based method which integrates the instantaneous velocity measured by PIV within the control volume and the pressure along control surfaces.

In this paper, we extend the previous efforts, first by measuring the instantaneous distribution of material acceleration for a high Reynolds number flow and then by integrating it over the entire flow field to measure the pressure distribution. The principles of the technique are described in the next section, followed in Sect. 3 by a demonstration of its validity using synthetic images. The experimental setup is presented in Sect. 4. During implementation, we have encountered a series of problems that affect the uncertainty in the measurements. In Sects. 5 and 6 we introduce solutions to these problems, including substantially improved techniques for matching images recorded by different cameras and for integrating the material acceleration. Sample results of pressure distribution measurements in a cavity turbulent flow are shown in Sect. 7.

## 2 Measurement of pressure distribution by integrating the material acceleration

Based on the Navier–Stokes equation, the pressure gradient can be expressed as

$$\nabla p = -\rho \left( \frac{D\vec{U}}{Dt} - \nu \nabla^2 \vec{U} \right). \quad (1)$$

Thus, if both the material acceleration,  $D\vec{U}/Dt$ , and the viscous terms,  $-\nu \nabla^2 \vec{U}$ , can be measured directly, the pressure  $p$  can be found by integrating Eq. 1. In a high Reynolds number flow field located away from boundaries, the material acceleration is dominant and the viscous term is negligible. As shown later in this paper, our experimental data for a cavity shear flow indeed confirms that the material acceleration is the dominant term. However, one should be careful to evaluate the contribution of the viscous term and avoid integrating along paths that are particularly affected by viscosity, e.g., along a boundary layer. Neglecting the viscous term, one has to measure the material acceleration and integrate it to determine the pressure.

The present technique for measuring the material acceleration is similar to the “pseudo-tracing” technique proposed by Jensen et al. (2003). To calculate the material acceleration, one has to compare the velocity of the same group of particles at two different times. We use two “cross-correlation” cameras to record four exposures of the particle traces within the sample area. The corresponding timings of the exposures are denoted as  $t_1, t_2, t_3$  and  $t_4$ , and there is an equal time interval,  $\delta t$ , between them. Camera 1 records images 1 and 3 and provides the first velocity distribution,  $\vec{U}_{13}$ , at  $t=t_2$ . Camera 2 records images 2 and 4 and generates the second velocity map,  $\vec{U}_{24}$ , at  $t=t_3$ . A particle group located at  $\vec{x}_a$  at  $t=t_2$  and has a velocity  $\vec{U}_{13}(\vec{x}_a, t_2)$  is located at  $\vec{x}_a + \vec{U}_a \delta t$  at  $t=t_3$ , where

$$\begin{aligned} & \vec{U}_a(\vec{x}_a + \vec{U}_a \delta t/2, t_2 + \delta t/2) \\ &= \frac{1}{2} (\vec{U}_{13}(\vec{x}_a, t_2) + \vec{U}_{24}(\vec{x}_a + \vec{U}_a \delta t, t_2 + \delta t)) \end{aligned} \quad (2)$$

is the averaged Lagrangian velocity of the same group of particles between  $t_2$  and  $t_2 + \delta t$ . This implicit expression requires (typically two) iterations during data analysis. The in-plane projection of the material acceleration at  $\vec{x}_a + \vec{U}_a \delta t/2$  and  $t=t_2 + \delta t/2$  can then be estimated as

$$\left. \frac{D\vec{U}}{Dt} \right|_{\vec{x}_a + \vec{U}_a \delta t/2, t_2 + \delta t/2} \approx \frac{\vec{U}_{24}(\vec{x}_a + \vec{U}_a \delta t, t_2 + \delta t) - \vec{U}_{13}(\vec{x}_a, t_2)}{\delta t}. \quad (3)$$

The velocity distribution at the same time can be estimated by averaging the two vector maps.

In our analysis, the velocity field  $\vec{U}_{13}$  and  $\vec{U}_{24}$  are obtained using an in-house developed PIV code. Its widely used version is described in Roth (1998) and Roth and Katz (2001), and a recent, substantially more accurate technique featuring correlation mapping method (abbreviated as CMM) is presented in Chen and Katz (2005). The latter eliminates the peak-locking error, thus achieving greater accuracy in measurements of

velocity gradients. This method, including the compensation of particle image distortion (Huang et al. 1993), is used for calculating the velocity in the present study.

For these procedures to work, the particles must remain within the laser sheet as the four exposures are recorded. Staggering the frames, i.e., calculating the first velocity field using exposures one and three ( $\vec{U}_{13}$ ) and the second velocity using exposures two and four ( $\vec{U}_{24}$ ) improves the chances that we indeed follow the same group of particles. In the present application, we choose the same time interval between exposures. However, the procedure would also work with varying intervals. The choice of  $\delta t$  must match the time scales of the flow and, within this constraint, increasing  $\delta t$  reduces the uncertainty of the acceleration measurement, consistent with Jensen and Pedersen (2004).

Integrating the planar projection of the material acceleration from a reference point with known pressure provides the pressure distribution  $p(\vec{x}, t_2 + \delta t/2)$ , as long as the viscous terms are small. At least two of the three components of the viscous term can also be evaluated, mostly to ensure that they are small. To minimize the effect of local acceleration errors, pressure is calculated using averaged, shortest path, virtual boundary, omnidirectional integration over the entire flow field, as discussed in detail in Sect. 6.

In the following section we implement this procedure to calculate the pressure distribution in synthetic flow fields and compare the computed and previously known pressure distributions. Note that if 3D data are available, e.g., from holographic PIV, one can calculate the local unsteady and convective terms of the acceleration at the same location. Using another approach, if the 3D velocity gradients are available, the instantaneous pressure distribution may be obtained by solving the Poisson equation,  $\nabla^2 p = -\rho(\partial u_i/\partial u_j)(\partial u_j/\partial u_i)$ , with appropriately prescribed boundary conditions. However, this approach is not suitable for 2D PIV-based data, since the third component of the velocity gradient is not available. One can also derive the measured projection of material acceleration to obtain a 2D Poisson equation, i.e.,

$$\frac{\partial^2 p}{\partial x^2} + \frac{\partial^2 p}{\partial y^2} = -\rho \left( \frac{\partial}{\partial x} \left( \frac{Du}{Dt} \right) + \frac{\partial}{\partial y} \left( \frac{Dv}{Dt} \right) \right).$$

However, this approach involves second derivatives of the measured velocity, and the resulting errors do not offer real advantage over direct spatial integration of the material acceleration. In a laminar flow, or to obtain the time-averaged pressure distribution for planar turbulent flows (2D in the mean), one can also solve the Poisson equation based on 2D PIV-based data as demonstrated by Gurka et al. (1999).

### 3 Proof of concept tests using synthetic images

To validate the principles of the pressure measurement technique, we use synthetic images of solid body rotation and stagnation point flows. The simulated seed

particles are distributed homogeneously in a  $2,048 \times 2,048$  pixels image using a random number generator available in Matlab. The particle concentration is set to maintain an average of 25 particles per interrogation window of  $32 \times 32$  pixels. The particle size has a Gaussian distribution, with a mean diameter of 2.4 pixels and a standard deviation of 0.8 pixels. The intensity of the particle image is based on the local integration result of a Gaussian intensity distribution with a peak grayscale of 240 to reflect the CCD sensor integration effect. Particle overlapping is avoided by identifying the occupied and unoccupied areas during the particle allocation process. Based on the first synthetic image, the subsequent three planes are generated by displacing the particles according to the local theoretical velocity, using the analytical expressions for the velocity fields. A bilinear interpolation is used for displacing the particles. The selected rotation rate of the synthetic solid body rotation is  $\omega = 0.0625 \text{ s}^{-1}$ , and the constant strain rate for the stagnation point flow is  $S = 0.025 \text{ s}^{-1}$ . The time interval between exposures is  $\delta t = 0.5 \text{ s}$ .

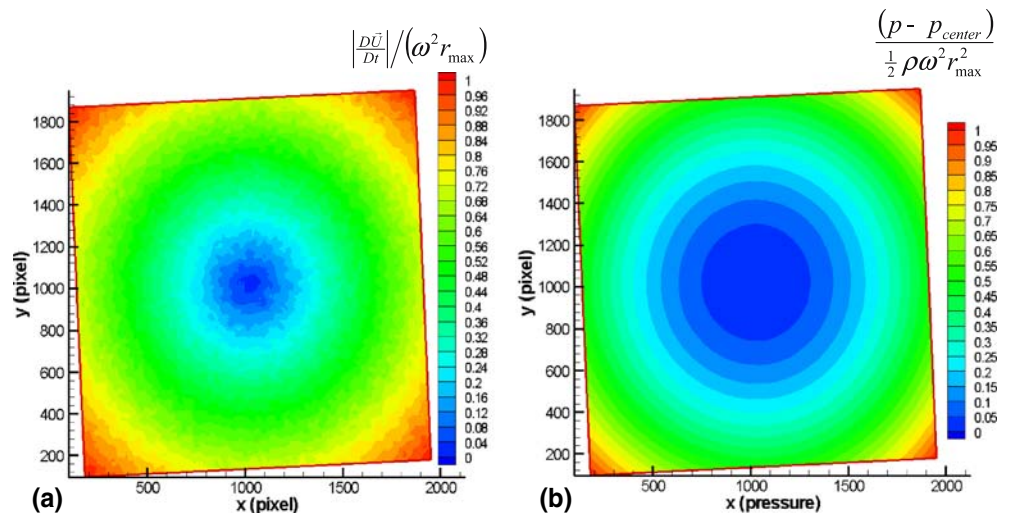
Figure 1a, b shows the material acceleration magnitude and the pressure distribution, respectively, for the solid body rotation. The irregularities in Fig. 1a are caused by errors that can be traced to the inherent uncertainty of the PIV analysis and by truncation errors. The irregularities disappear in the pressure distribution contours due to the omni-directional integration that acts as a low-pass filter. The measured radial pressure distribution is compared to the theoretical values in Fig. 2. The degree of agreement is self-evident. The difference between the measured and the theoretical pressures has a standard deviation of 1.05%. Note that 70% of this error is caused by positioning the velocity vectors in the middle of the interrogation window of the first exposure, i.e., without accounting for the displacement. For the synthetic stagnation point flow (data not shown), the standard deviation is 1.03%.

In examining contributors to overall uncertainty, we have isolated the effects of each step using exact data. For example, to examine the effect of integration, we have used the exact values of acceleration and determined the error in pressure. The analysis indicates that the uncertainty is dominated by errors in velocity measurements. The contribution of any other steps in the procedure is at least an order of magnitude smaller. To quantify the effects of error in velocity, we have imposed random errors with a standard deviation of 0.5, 0.3 and 0.1 pixels to the exact velocities of the rotational flow. The corresponding standard deviations from the exact pressures are 2.9, 2.2 and 1.4% when normalized by the local pressure. This relative error is dominated by values near the center of the simulated vortex, where the local pressure is low. If the error is normalized by the difference between the maximum and minimum pressures, the corresponding standard deviations of errors are 0.4, 0.4 and 0.2%, respectively. However, these low values are affected by the high range of displacement in the simulated vortex, 83 pixels at the outer perimeter and almost zero near the center. Experimental data with lower displacement range between exposures will have higher errors. This error analysis is only preliminary. We will follow with a detailed study based on DNS data.

#### 4 Experimental and optical setup

The pressure measurement technique is applied to a cavity shear flow in a small water tunnel, which is described in Gopalan and Katz (2000). Since the primary objective of this paper is to introduce a new technique, we do not focus on the physics of this flow. The reader can refer to Tang and Rockwell (1983), Lin and Rockwell (2001) and Rockwell and Knisely (1979) for background on the studies of shear layers above cavities. The optical setup together with the test facility and model is sketched in Fig. 3. The 38.1 mm long,

**Fig. 1** **a** Magnitude of the material acceleration and **b** spatial pressure distribution integrated from the material acceleration for the synthetic rotational flow





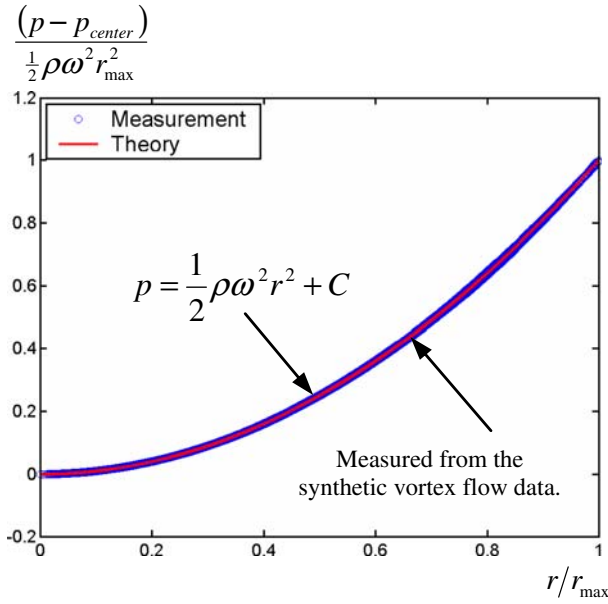


Fig. 2 Radial pressure distribution for the synthetic rotational flow

50.8 mm wide and 30.0 mm deep 2D cavity is installed in the  $50.8 \times 63.5 \text{ mm}^2$  test section. As shown, the test model has a contraction ramp leading to the cavity and a diffusing ramp downstream of the cavity. A 13 mm long region with tripping grooves having a notch depth of 0.46 mm and opening of 1.00 mm is machined at the beginning of the contraction ramp in order to trip the boundary layer.

To record the four exposures we use two  $2K \times 2K$  cross-correlation digital cameras with interline image transfer (Kodak ES4.0). The light sources are two dual-head Nd:Yag lasers (New Wave MiniLase 15 and III-15,

15 mJ/pulse at 532 nm, pulse width 5–7 ns), with flashes 1 and 3 generated by laser No. 1 and flashes 2 and 4 by laser No. 2. The time interval  $\delta t$  between the laser flashes is 25  $\mu\text{s}$ . A half-wave plate is used for rotating the polarization of laser No. 1 before mixing the beams and expanding them to sheets. Consequently, the polarization direction of the light in pulses 1 and 3 is perpendicular to that of pulses 2 and 4. As discussed in Christensen and Adrian (2002), most of the light reflected from tracer particles (hollow, 8–12  $\mu\text{m}$ , glass spheres with specific gravity of 1.05–1.15) located within the laser sheet maintains its polarization angle. Thus, by placing a polarizing beam splitter (cube) in front of the cameras, we can separate images 1 and 3 from images 2 and 4 and direct them onto their respective cameras.

To maximize the spatial resolution of the acceleration measurements, we use progressive grid refinement, culminating in  $16 \times 16$  pixels interrogation window with 50% overlap between windows. The corresponding length scales for a  $50.8 \times 50.8 \text{ mm}^2$  field of view are an interrogation window of  $0.4 \times 0.4 \text{ mm}^2$  and vector spacing of 0.2 mm. Thus, the present spatial resolution extends well into the turbulence dissipation scales. However, when the vector spacing and the interrogation window size are much larger than the dissipation scales, one must examine the effect of the sub-grid scale stresses on the momentum balance since they may become significant. At the present resolution they are not. In this paper, the pressure distributions are presented in terms of pressure coefficient,  $C_p = (p - p_{\text{ref}}) / ((1/2)\rho U_e^2)$ , where  $p$  is the measured pressure,  $p_{\text{ref}}$  the reference pressure and  $U_e$  the external free stream velocity above the cavity.

## 5 Vector alignment based on local deformation correction

It is essential to match the fields of view of the two cameras, requiring an elaborate alignment and calibration process. As a result, camera 1 is installed on a three-axis translation stage, while camera 2 is installed on a tilt and rotation stage (see Fig. 3). A target with grid (Edmund Industrial Optics, model NT46–250), illuminated using incandescent light source, is placed in the test section. The plane of the target is aligned with the laser sheet to the best of our ability, considering that the sheet has a finite depth. The two images of this target are compared, and the differences between them are minimized by iteratively adjusting the focus of the lens and the settings of the mounting stages.

However, mechanical alignment is insufficient. For example, for the  $25.4 \times 25.4 \text{ mm}^2$  field of view of a  $2K \times 2K$  camera with  $\delta t = 25 \mu\text{s}$ , a 0.05 mm misalignment in the lateral direction in the target plane results in a displacement of 4 pixels on the image plane, i.e., an increase of relative velocity by 1.0 m/s, which corresponds to an acceleration error of 40,000  $\text{m/s}^2$ , an unacceptable level. To overcome this problem, similar to

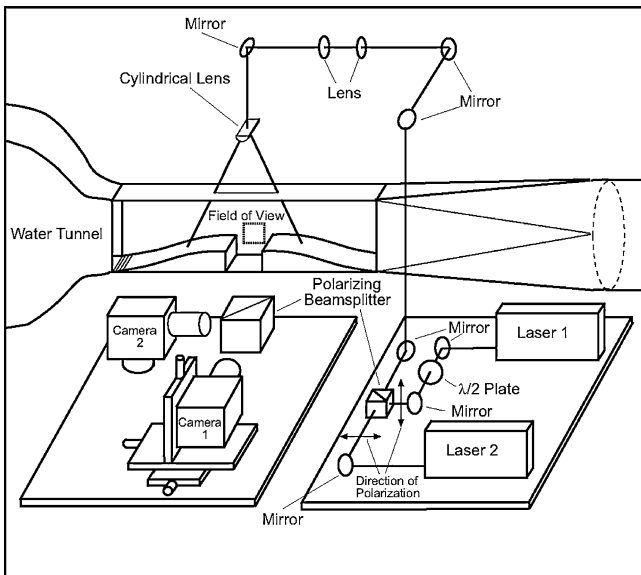


Fig. 3 Optical setup

Jensen et al. (2001), we also compare images of a densely seeded flow which are acquired at the same time by triggering both lasers simultaneously. The images are analyzed like a typical PIV pair to determine the spatial distribution of relative displacement between the two images. Based on the information about the relative displacement, we have tried several methods for matching the two fields of view including: (a) *decomposition* of relative displacements into relative translation, rotation and magnification (Liu and Katz 2003, 2004); (b) *global mapping* of distortion using polynomials of different orders; and (c) *local deformation correction*, as will be described shortly. In spite of considerable effort, the first two approaches have failed to match the local deformations at levels below 0.1 pixel. Due to the sensitivity of pressure measurements to camera misalignment, a bias error in velocity on the order of 0.1–0.5 pixels leads to substantial errors in pressure. The local deformation correction method has solved our problem by providing the most accurate matching, so it is described in detail below.

As illustrated in Fig. 4, suppose  $O(x_0, y_0)$  and  $P(x, y)$  are the starting and ending points of a vector  $\vec{OP}$  on camera 1, where  $\vec{OP} = (x - x_0, y - y_0) = (u_{c1}, v_{c1}) = \vec{V}_{C1}$ . Correspondingly, the same vector on camera 2 is denoted as  $\vec{O'P'} = (x' - x'_0, y' - y'_0) = (u_{c2}, v_{c2}) = \vec{V}_{C2}$ , with  $O'$  ( $x'_0, y'_0$ ) and  $P'$  ( $x', y'$ ) being the starting and ending points, respectively. Here,  $u$  and  $v$  represent velocity components, and  $c_1$  and  $c_2$  refer to a specific camera. The relative displacement between  $O(x_0, y_0)$  and  $O'$  ( $x'_0, y'_0$ ) is  $\vec{D}_0 = (D_{x0}, D_{y0})$  and between  $P(x, y)$  and  $P'$  ( $x', y'$ ) is  $\vec{D} = (D_x, D_y)$ . With Taylor expansion of  $D_x$ , one obtains

$$\begin{aligned} x' - x'_0 &= (x + D_x) - (x_0 + D_{x0}) \\ &= (x - x_0) + (x - x_0) \frac{\partial D_x}{\partial x} \bigg|_{x_0, y_0} \\ &\quad + (y - y_0) \frac{\partial D_x}{\partial y} \bigg|_{x_0, y_0} + \frac{1}{2} \left[ (x - x_0)^2 \frac{\partial^2 D_x}{\partial x^2} \bigg|_{x_0, y_0} \right. \\ &\quad + 2(x - x_0)(y - y_0) \frac{\partial^2 D_x}{\partial x \partial y} \bigg|_{x_0, y_0} \\ &\quad \left. + (y - y_0)^2 \frac{\partial^2 D_x}{\partial y^2} \bigg|_{x_0, y_0} \right] + \text{H.O.T.} \end{aligned} \quad (4)$$

i.e.,

$$\begin{aligned} u_{c2} &= u_{c1} + u_{c1} \frac{\partial D_x}{\partial x} \bigg|_{x_0, y_0} + v_{c1} \frac{\partial D_x}{\partial y} \bigg|_{x_0, y_0} \\ &\quad + \frac{1}{2} \left[ u_{c1}^2 \frac{\partial^2 D_x}{\partial x^2} \bigg|_{x_0, y_0} + 2u_{c1}v_{c1} \frac{\partial^2 D_x}{\partial x \partial y} \bigg|_{x_0, y_0} + v_{c1}^2 \frac{\partial^2 D_x}{\partial y^2} \bigg|_{x_0, y_0} \right] \\ &\quad + \text{H.O.T.} \end{aligned} \quad (5)$$

Similarly, we get

$$\begin{aligned} v_{c2} &= v_{c1} + u_{c1} \frac{\partial D_y}{\partial x} \bigg|_{x_0, y_0} + v_{c1} \frac{\partial D_y}{\partial y} \bigg|_{x_0, y_0} \\ &\quad + \frac{1}{2} \left[ u_{c1}^2 \frac{\partial^2 D_y}{\partial x^2} \bigg|_{x_0, y_0} + 2u_{c1}v_{c1} \frac{\partial^2 D_y}{\partial x \partial y} \bigg|_{x_0, y_0} + v_{c1}^2 \frac{\partial^2 D_y}{\partial y^2} \bigg|_{x_0, y_0} \right] \\ &\quad + \text{H.O.T.} \end{aligned} \quad (6)$$

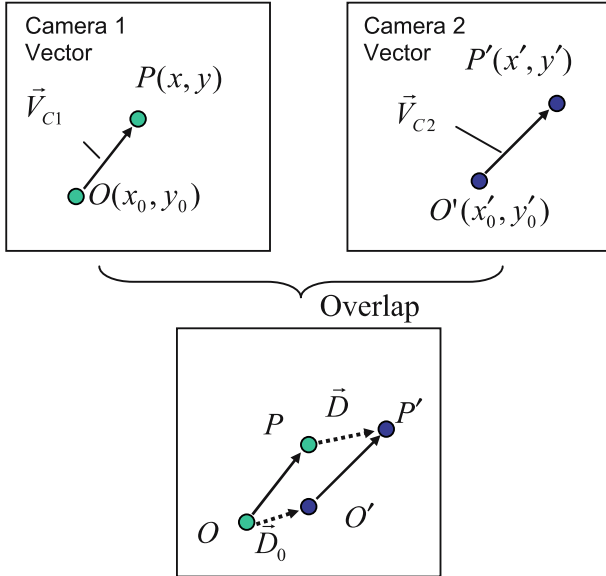
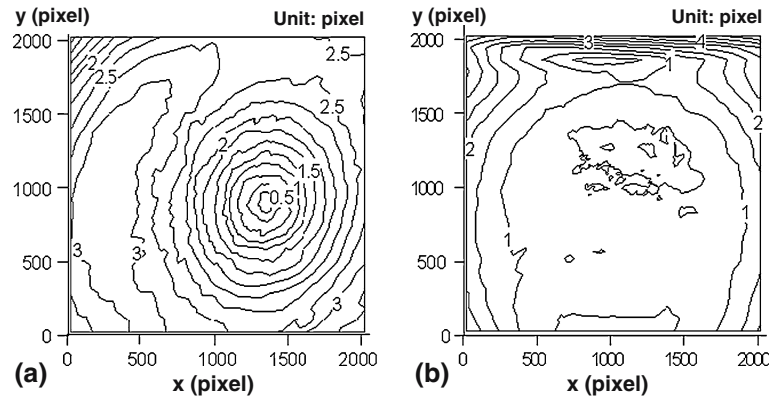


**Fig. 4** Schematic illustration of two velocity vectors, which are supposed to be identical, but are different due to mismatches in location, magnification and deformation in the images recorded by camera 1 and camera 2

The distribution of  $\vec{D}(x, y)$  is available from the cross-correlation of images recorded by both cameras at the same time. Using Eqs. 5 and 6, the camera 1 velocity vector components can be aligned to those of camera 2. The corresponding camera 2 velocity components at the same physical location can be obtained using interpolation at places indicated by  $\vec{D}(x, y)$ . The resulting grid on camera 2 is slightly irregular. Following these corrections, the resulting vector maps contain mostly errors due to lens-induced distortion of *one* camera. However, calibrations using the target show that this distortion is less than 0.003 pixel per pixel, much smaller than the typical accuracy of the PIV cross-correlation analysis (on the order of 0.1 pixel). Consequently, the effect of image distortion imbedded in the velocity is not a primary concern.

To gauge the accuracy of the above three velocity vector alignment methods, we distort a pair of synthetic images of the solid body rotation described in Sect. 3 using two sets of spatial distortion function, which are based on measured (real) calibration images of a grid target, as shown in Fig. 5. The distortions extend to 3 pixels at the perimeter of the images, and their spatial

**Fig. 5** Iso-contours of magnitude of relative displacement between a grid target and the two cameras: **a** camera 1; **b** camera 2



distributions in the two images differ. The distorted velocity vectors of camera 1 are then aligned to the distorted velocity of camera 2 using the aforementioned procedures. The statistics of the differences in velocity ( $\delta u$  and  $\delta v$ ) after the matching procedures are presented in Table 1. Decomposition of the relative displacement introduces a large and unacceptable level of error. The global mapping method and the local deformation correction based on standard PIV procedures (Roth 1998; Roth and Katz 2001) have standard deviation of less than 0.1 pixel. As illustrated later, the resulting bias was unacceptable for pressure measurements. The first and second order local deformation correction, used together with the PIV analysis code based on the CMM (Chen and Katz 2005), gives the most accurate alignment result. A standard deviation of 0.01 pixels (six times less than the other methods already, at least for synthetic images) reduces the bias associated with image matching to an acceptable level. Furthermore, the local corrections minimize bias errors that occur when a continuous function is fitted to discrete data.

To illustrate the impact of the new procedures on the pressure distributions, Fig. 6 compares the instantaneous pressure distributions of the cavity shear layer calculated using the same velocity data, but different methods for matching the two fields of view. The distribution calculated using the sixth order polynomial fit

(left side), with its bias error not exceeding 0.2 pixels, clearly displays unrealistic pressure peaks above the shear layer, especially along the upper right side of the distribution, where the flow is quite uniform. The high negative peaks along the right cavity wall below the shear layer is also unrealistic, considering the magnitudes of velocity there. This bias disappears when we use second order local deformation correction.

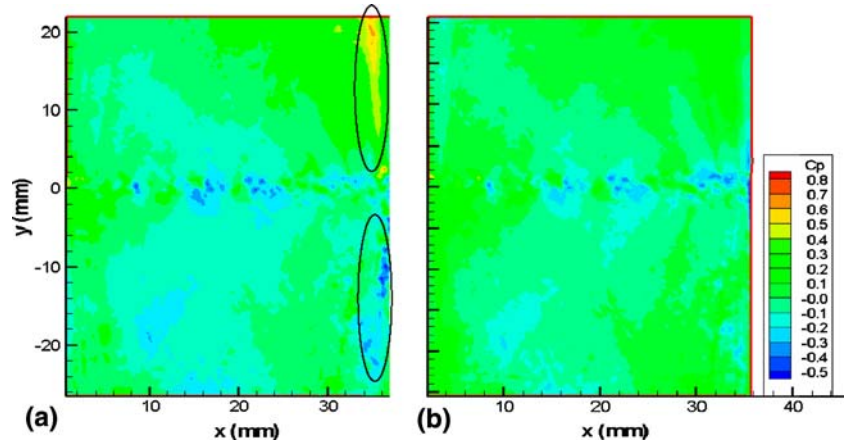
## 6 Pressure integration algorithm

With the material acceleration measured at discrete nodal points in a planar flow field, the pressure can be reconstructed by solving a least square problem. For a sample grid, at each nodal point there are two known components of the material acceleration and one unknown variable, the pressure. These variables are related to each other via discrete differential equations, which form an over-determined matrix equation. The three primary ways to solve this matrix equation are: matrix iteration (Southwell 1980), direct matrix inversion (Herrmann 1980) and singular value decomposition (Press et al. 2002). However, the matrix iteration method results are sensitive to the initial value setting, and use of a relaxation factor requires experience. The direct matrix inversion and singular value decomposition

**Table 1** Comparison of accuracy of velocity vector alignment methods based on distorted synthetic images

	Standard deviation of $\delta u$ (pixel)	Standard deviation of $\delta v$ (pixel)	Mean $\delta u$ (pixel)	Mean $\delta v$ (pixel)
Decomposition of camera image relative displacement	0.169	0.206	-0.153	0.229
Sixth order polynomial global mapping	0.078	0.078	-0.00076	0.00111
First order local deformation correction using the code of Roth and Katz (2001)	0.0613	0.0682	-0.00046	0.00099
Second order local deformation correction using the code of Roth and Katz (2001)	0.0625	0.0688	-0.0016	-0.0005
First order local deformation correction using the code of Chen and Katz (2005)	0.0112	0.0109	0.00066	-0.00048
Second order local deformation correction using the code of Chen and Katz (2005)	0.0107	0.0105	-0.00029	-0.00017

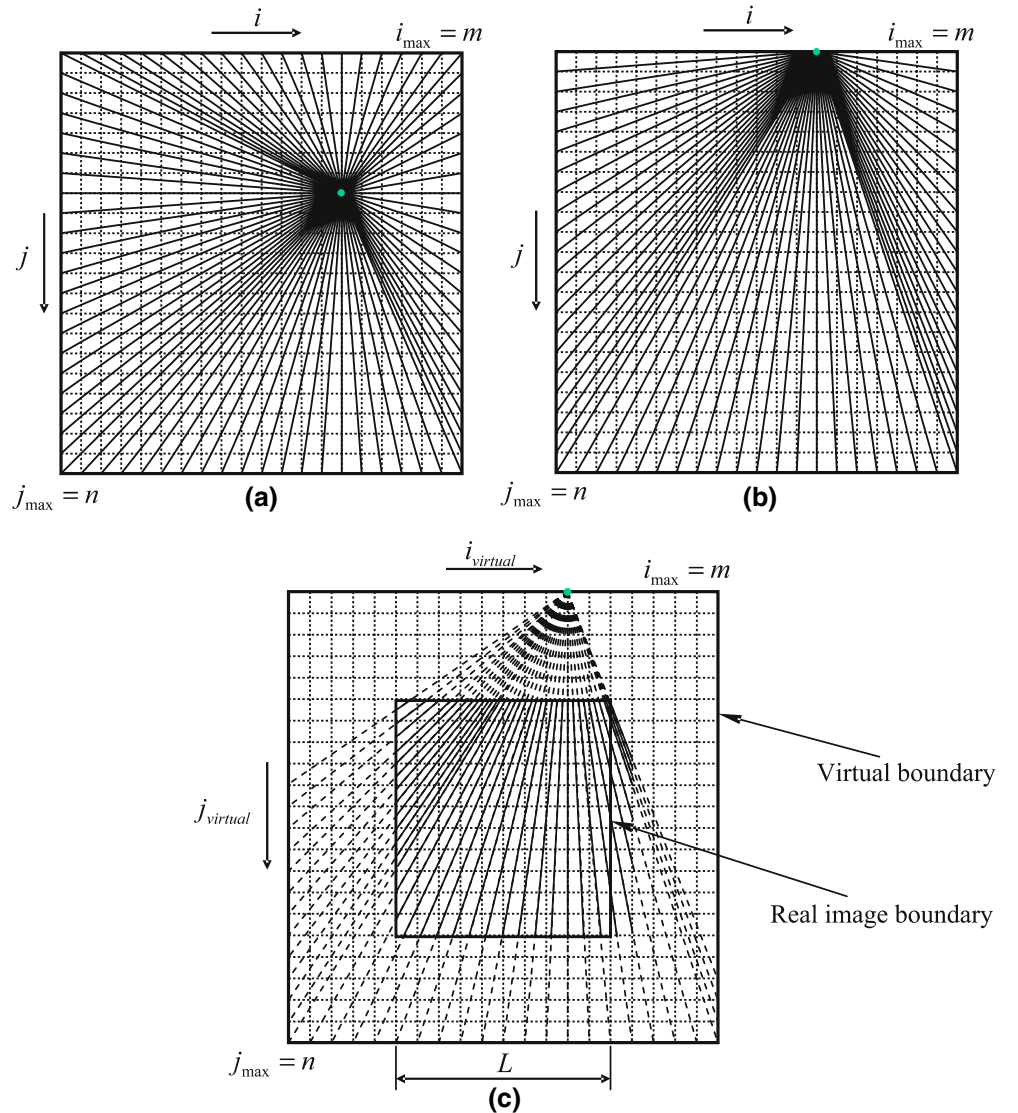
**Fig. 6** A comparison between pressure distributions calculated using the same data, but different methods for matching the two fields of view. **a** Matching by polynomial fit; **b** matching by second order local deformation correction using the CMM PIV method. The sample area extends from the leading edge (0,0) to the trailing edge (38,0) of the cavity



approaches must involve the full matrix during computation. For a grid with  $220 \times 220$  nodes, which is typical for PIV analysis using  $2K \times 2K$  cameras, the largest storage requirement of a full matrix when solving the

matrix equation is 18 GB, which is impractical at the current level of computer technology. To bypass these limitations, we developed a simpler algorithm for direct integration.

**Fig. 7** Pressure gradient integration algorithms: **a** averaged, shortest path, omni-directional integration; **b** omni-directional paths originated and ending at boundaries; **c** virtual boundary omni-directional integration algorithm





Since pressure is a scalar field, the integration of pressure gradients must be independent of the integration path. To minimize the effect of the error in the acceleration field, we first implemented a method featuring *averaged, shortest path, omni-directional integration* over the entire flow field. An illustration of the integration paths used initially is presented in Fig. 7a. Starting from the top left corner, we first integrate the acceleration along the boundary. To determine the pressure at a certain internal point, we then integrate the acceleration along nearly straight paths (shortest paths) from each of the boundary point to the internal node and then average all the integration results. For an  $m \times n$  grid, the number of boundary nodes is  $2(m+n)$ . Thus, the total number of integration paths needed for calculating the pressure over the entire domain is  $2(m+n)mn$ . For  $m=n=250$ , the number of paths is  $62.5 \times 10^6$ . Such a large number is prohibitively expensive, especially considering that one may wish to perform thousands of measurements to obtain converged statistics on the pressure field and pressure-velocity correlations.

To solve this problem, we switched to an equivalent, but more efficient, *modified omni-directional integration* algorithm, as illustrated in Fig. 7b. Instead of focusing on the internal nodes, we focus on the boundary, and integrate from each of the boundary node to all the other boundary nodes. As the integration path crosses a certain internal node, the result of integration is stored in a data bin associated with this node. Repeating this procedure for all the boundary nodes results in multi-direction integration for each internal node. This process substantially reduces redundant integration paths. The

total number of integration paths for an  $m \times n$  grid is reduced to  $2m(n+m) + 2n(2m+n)$ , i.e.,  $0.75 \times 10^6$  for  $m=n=250$ , almost two orders of magnitude less than the original procedure. Implementing this method using a single processor, mid-range Pentium PC provides the pressure distribution in about 4 min—not yet an optimum ( $< 1$  min is desirable), but already manageable. After using this procedure for a while, we realized that we have to resolve two major problems.

First, as illustrated in Fig. 8, the number of times a certain node is crossed during the omni-directional integration is not uniform in the circumferential direction and varies depending on the location in the sample area. Integration to nodes located close to the center gives similar weight to all directions, while integration to nodes located near the boundaries, as shown, involves non-uniform utilization of integration paths. Errors and bias would be an inherent outcome.

The second problem is the adverse effects of error in pressure along the boundary that results from the accumulation of acceleration errors during the initial integration along the boundary. The velocity and acceleration in boundary points is typically the least accurate, primarily due to the higher image deformation along its edges. Since each integration path starts at the boundary, the boundary errors have sustained effect on all the data.

To solve these problems, we have made the following changes. First, we introduced the *virtual boundary integration method*, which is illustrated in Fig. 7c. The integration still starts from and stops at the real boundaries, but instead of following paths originating from real boundaries, this time the integration proceeds along paths originating from the virtual boundaries that extend beyond the real boundaries. Consequently, all the nodal points of interest are now located away from the boundary, preventing the path clustering shown in Fig. 8.

Second, to reduce the effect of erroneous pressure along the boundary we use iterations and include the boundary nodes in the integration process. Initially, we still integrate along the perimeter, but since each boundary node is crossed by numerous paths, the initial boundary values can be corrected/replaced with the results of the omni-directional integration. The integration process is then repeated using the new boundary values and the iterations proceed until the results converge or the variations between iterations decrease to below an acceptable threshold level. Note that the incremental changes in pressure within the sample area, i.e., the values of the material acceleration, do not change. However, the pressure at each point changes as the values of pressure along the boundary are updated in each step. The mean difference in pressure over the entire sample area after each iteration for a sample cavity shear flow data,  $\Delta p$ , is presented in Fig. 9 for three different gaps between the real and virtual boundaries. The gap is expressed in terms of  $L$ , the length of the real grid size. For a gap of  $0.5L$ , the mean variation in pressure between the first and the

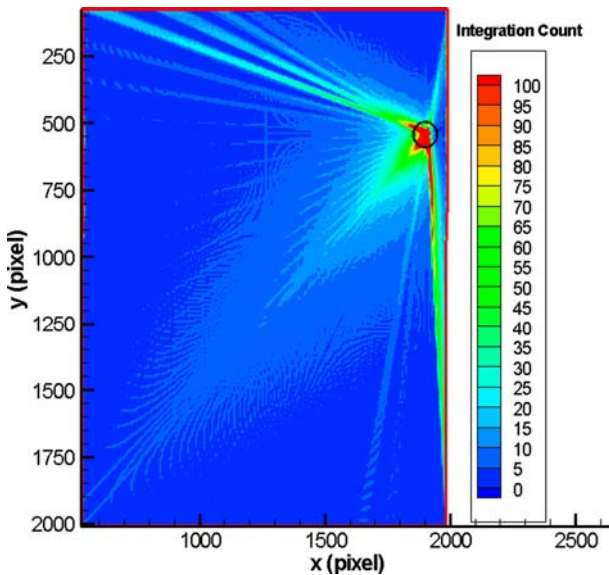
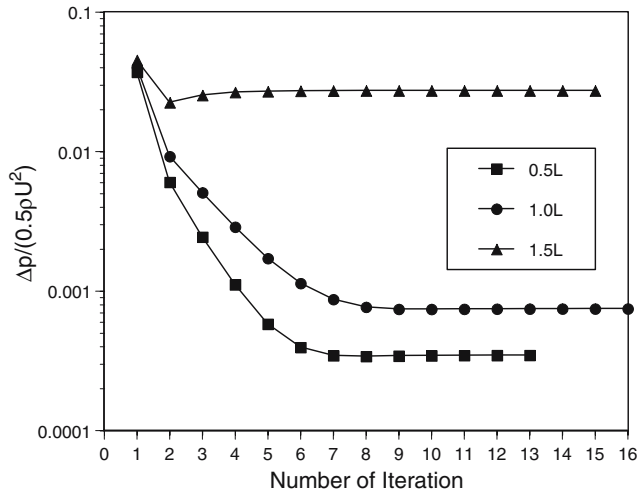


Fig. 8 Distribution of the number of times a certain node is used for calculating the pressure at the encircled node using integration paths originated from the real boundaries (i.e., algorithm b in Fig. 7). For points located near the center of the sample area, the distribution is uniform. For points located near the boundary, the distribution is not uniform



**Fig. 9** Convergence test of the virtual boundary iteration algorithm for cavity shear layer flow showing the mean difference in pressure after each iteration

second iterations is less than 5% of the dynamic head, but it decreases to less than 0.04% of the dynamic pressure after seven iterations. The number of iterations required to obtain converged results decreases with increasing gap, since the rearrangement of integration paths is equivalent to allocation of weights in the multi-directional integration. With increasing gap between virtual and real boundaries, the weight allocation becomes more balanced, achieving a quicker rate of convergence. However, more balanced weight with increasing gap may not necessarily guarantee an improved mixing of nodal points during integration and may even result in a higher residue error. It seems that for the present data the optimum gap is somewhere in the  $0.5L$ – $1.0L$  range. However, we need to gain more experience in order to identify an optimum.

A similar analysis using the synthetic images leads to similar trends (not shown).

The impact of the new procedure and iterations on the instantaneous pressure distribution is demonstrated in Fig. 10. The pressure distribution based on omnidirectional integration starting from real boundaries is shown in Fig. 10a. Using the boundary data obtained from this integration as the initial input for the first iteration of virtual boundary integration gives the result shown in Fig. 10b. The pressure distribution after the tenth iteration of virtual boundary integration is shown in Fig. 10c. For this example, the average pressure difference before and after the first round of virtual boundary integration is 7.5% of the maximum pressure value, i.e., the initial correction is substantial. After ten iterations, the pressure difference between iteration decreases to 0.04% of the dynamic pressure, i.e., to insignificant levels. As is evident, the pressure distributions in Fig. 10b differ significantly from Fig. 10a in several regions, especially along the boundaries. The extended virtual boundary greatly reduces the bias in integration path, and the iterations eliminated the dependence on the initial integration along the outer perimeter of the sample area.

## 7 Sample pressure distributions

In the samples presented below, the origin of the coordinates is placed at the leading edge of the cavity. To illustrate the overall flow structure, Fig. 11a shows a sample instantaneous velocity distribution and streamlines. Here, the mean velocity in the nearly potential flow above the cavity is 10 m/s and the Reynolds number is 335,000 based on the cavity length. The thickness of the shear layer is around 2 mm. Due to the oscillation of the shear layer, the stagnation point of the flow on the

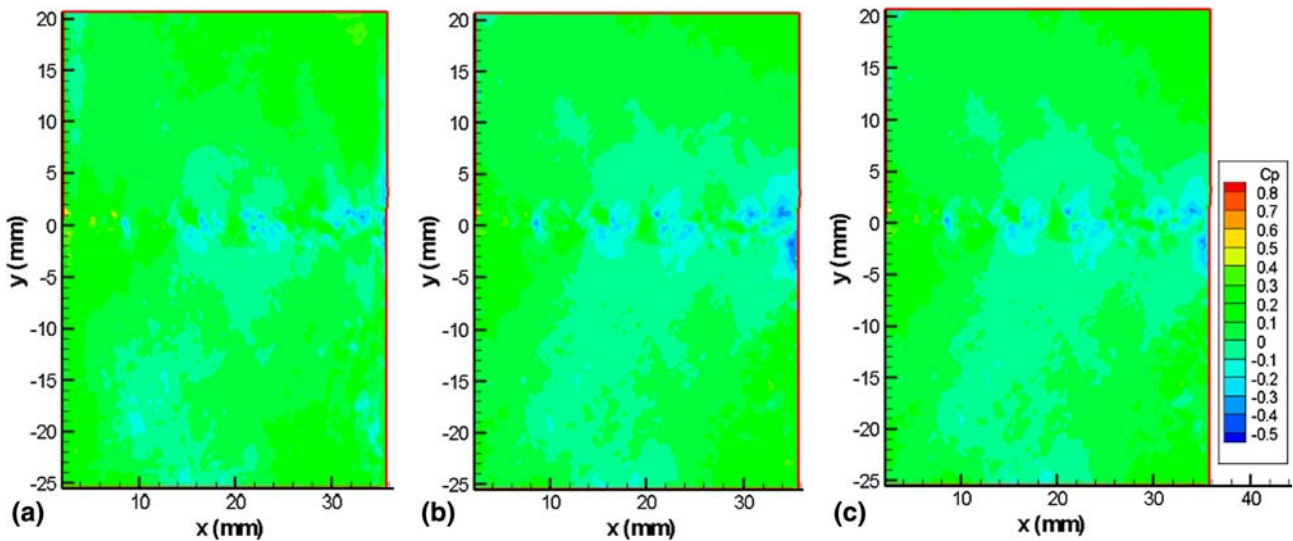
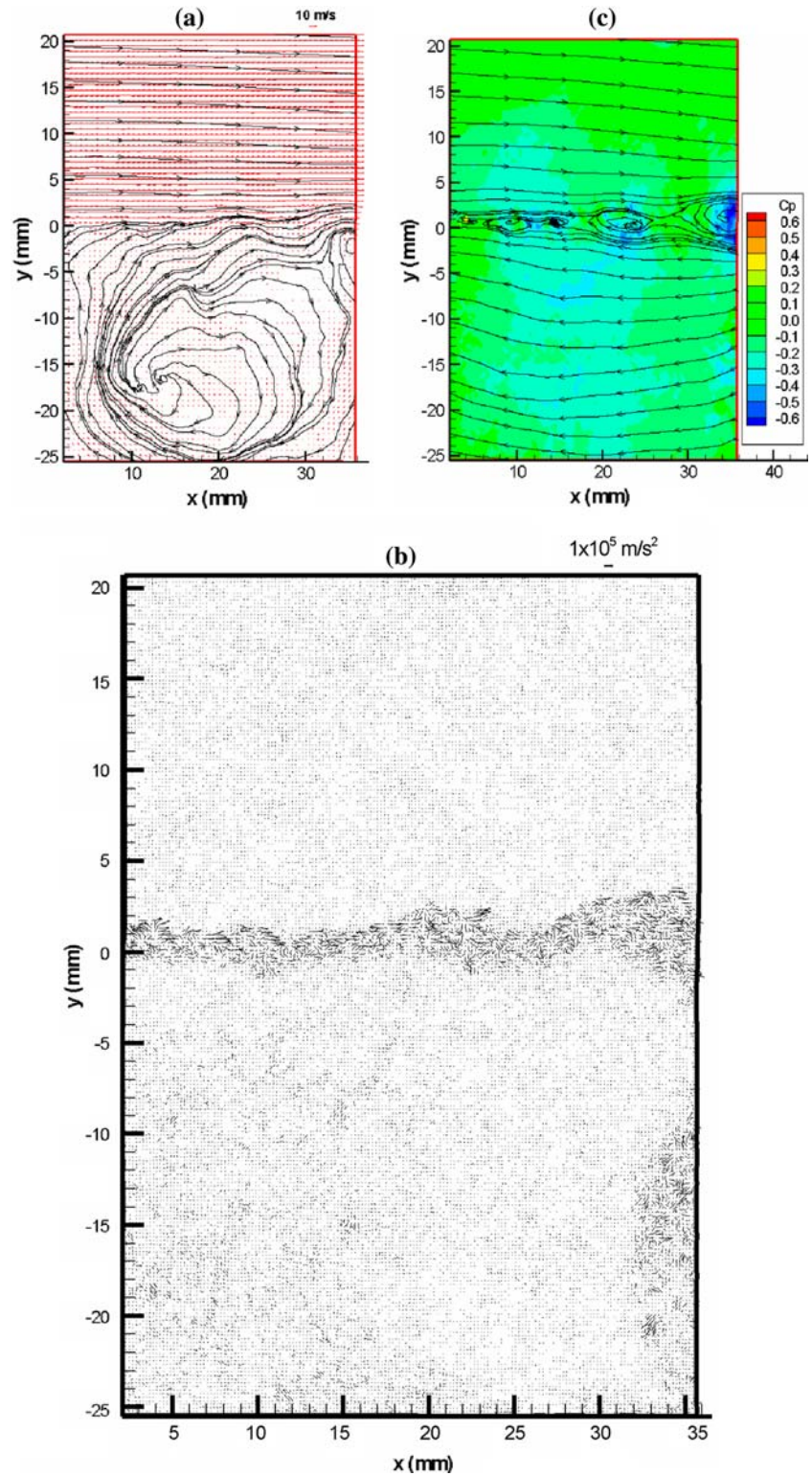


**Fig. 10** Comparison of pressure distribution obtained using different integration schemes. **a** Integration starting from real boundaries; **b** first round of virtual boundary integration; **c** after ten iterations of virtual boundary scheme

**Fig. 11** Sample results for instantaneous cavity shear flow at  $U_e = 10$  m/s and  $Re = 335,000$ . **a** Streamlines; **b** material acceleration; **c** pressure distribution with streamlines based on a reference frame moving downstream at half of the mean velocity above the cavity



downstream wall of the cavity varies significantly from one instantaneous realization to the next (Lin and Rockwell 2001; Rockwell and Knisely 1979). In Fig. 11a, the stagnation point is located about 4 mm below the trailing edge corner. Below the shear layer, there is a recirculation zone, which contains remnants of

vorticity swept down from the shear layer. The maximum velocity in the recirculation region is only about 30% of the free stream velocity.

Following the procedures outlined in this paper, we calculate the instantaneous distribution of material acceleration, which is shown in Fig. 11b and then integrate



it to obtain the pressure distribution, presented in Fig. 11c. The local pressure at the upper left corner is selected as the reference level. The streamlines are based on a reference frame moving at half of the external velocity to show the pseudo-vortical structure. The maximum magnitude of the material acceleration is around  $80,000 \text{ m/s}^2$ , which is on the same order of magnitude as that obtained by La Porta et al. (2001) for a coaxial counter-rotating disk turbulent flow. The material acceleration vectors appear to congregate as converging/diverging clusters in the shear layer. As expected, high pressure develops in regions of flow deceleration, and conversely, pressure minima develop in accelerating regions. Both regions are located mainly within the shear layer. However, some of these pressure maxima /minima appear to have global effects over the entire flow field. Additional samples of instantaneous pressure distribution are shown in Fig. 12. Clearly, the instantaneous pressure field varies dramatically due to

the oscillation of the shear layer. Though not presented here, our results indicate that the temporal derivative of velocity is typically higher than the convection terms as the major contributing term to the material acceleration.

As for the magnitude of the viscous term, evaluation of our data of the cavity shear layer confirms that the in-plane instantaneous viscous terms are typically three orders of magnitude smaller than the acceleration term. The average difference in the final pressure distribution with and without the viscous term is only 0.008% of the dynamic pressure.

## 8 Conclusions

This paper introduces a non-intrusive technique for measuring the instantaneous spatial distribution of pressure by integrating the measured distribution of material acceleration. To measure the in-plane projection of the

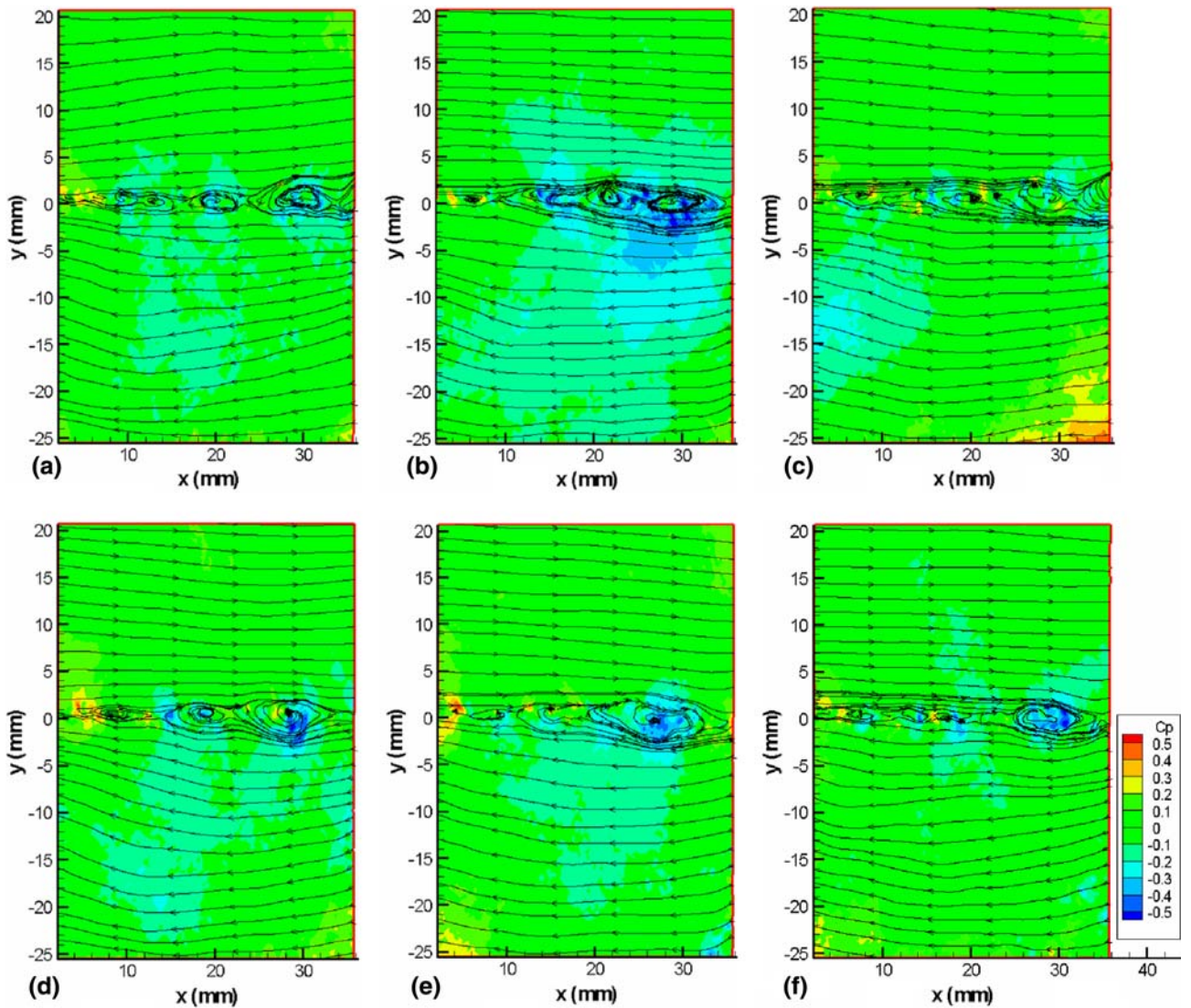


Fig. 12 Sample instantaneous pressure distributions of the cavity shear flow



material acceleration, the technique compares the velocity of the same group of particles at different times, similar to Jensen et al. (2003). The principles of the procedure are validated using synthetic rotational and stagnation point flows. The standard deviation of the measured instantaneous pressure from the theoretical value is about 1.0%. Experimentally, the method consists of recording four exposures of the particle field. A key to the success of the application of this technique in an experimental setup is the precise matching of the two fields of view. A local deformation correction method is introduced. This technique maps the velocity field measured by one camera onto the other based on the measured spatial distribution of the same particle field as recorded by both cameras simultaneously. This alignment method reduces the standard deviation of velocity differences due to relative misalignment and distortion to about 0.01 pixels in synthetic images. An omni-directional virtual boundary integration scheme is used to integrate the spatial distribution of acceleration. Multi-integration paths minimize the effect of local random errors in acceleration. Further improvements are achieved by iterations to correct the pressure along the boundary. Typically 3–5 iterations are sufficient for reducing the incremental mean pressure change in each iteration to less than 0.1% of the dynamic pressure. This technique has been used for pressure measurements in a cavity turbulent shear flow and sample results are provided. On-going research will provide statistics on the velocity–pressure gradient tensor. Combined with cavitation inception tests, we will also examine the relationship between pressure fluctuations and the onset of cavitation.

The local deformation correction method may be used for image alignment in circumstances where two cameras record the same field of view. Although the present pressure measurement technique is based on 2D PIV technology, the procedures can be readily extended to 3D holographic PIV applications.

**Acknowledgements** This work is sponsored by the Office of Naval Research of the United States (Program Officer Dr. Ki-Han Kim). The authors would like to thank Yury Ronzhin for the mechanical design of the testing body and Stephen King for building the timing control device. Bo Tao's participation at the initial stage of this project and Shridhar Gopalan and Jun Chen's valuable assistance are also gratefully acknowledged.

## References

- Arndt REA (2002) Cavitation in vortical flows. *Annu Rev Fluid Mech* 34:143–175
- Blake WK (1986) *Mechanics of flow-induced sound and vibration*. Academic, New York
- Brennen CE (1995) *Cavitation and bubble dynamics*. Oxford University Press, Oxford
- Chang K-A, Liu PL-F (1998) Velocity, acceleration and vorticity under a breaking wave. *Phys Fluids* 10:327–329
- Chang K-A, Cowen EA, Liu PL-F (1999) A multi-pulsed PTV technique for acceleration measurement. In: *International workshop on PIV'99—Santa Barbara, 3rd, Santa Barbara, CA, USA, 16–18 September 1999*, pp 451–456
- Chen J, Katz J (2005) Elimination of peak-locking error in PIV analysis using the correlation mapping method. *Meas Sci Technol* 16:1605–1618
- Christensen KT, Adrian RJ (2002) Measurement of instantaneous Eulerian acceleration fields by particle-image velocimetry: method and accuracy. *Exp Fluids* 33:759–769
- Dong P, Hsu TY, Atsavapranee P, Wei T (2001) Digital particle image accelerometry. *Exp Fluids* 30:626–632
- Girimaji SS (2000) Pressure-strain correlation modeling of complex turbulent flows. *J Fluid Mech* 422:91–123
- Gopalan S, Katz J (2000) Flow structure and modeling issues in the closure region of attached cavitation. *Phys Fluids* 12:895–911
- Gurka R, Liberzon A, Hefetz D, Rubinstein D, Shavit U (1999) Computation of pressure distribution using PIV velocity data. In: *International workshop on PIV'99—Santa Barbara, 3rd, Santa Barbara, CA, USA, 16–18 September 1999*, pp 671–676
- Gutmark E, Wygnanski I (1976) The planar turbulent jet. *J Fluid Mech* 73:465–495
- Herrmann J (1980) Least-squares wave front error of minimum norm. *J Opt Soc Am* 70:28–35
- Huang HT, Fiedler HE, Wang JJ (1993) Limitation and improvement of PIV, part II: particle image distortion, a novel technique. *Exp Fluids* 15:263–273
- Jakobsen ML, Dewhurst TP, Greated CA (1997) Particle image velocimetry for predictions of acceleration fields and force within fluid flows. *Meas Sci Technol* 8:1502–1516
- Jensen A, Pedersen GK (2004) Optimization of acceleration measurements using PIV. *Meas Sci Technol* 15:2275–2283
- Jensen A, Sveen JK, Grue J, Richon J-B, Gray C (2001) Accelerations in water waves by extended particle image velocimetry. *Exp Fluids* 30:500–510
- Jensen A, Pedersen GK, Wood DJ (2003) An experimental study of wave run-up at a steep beach. *J Fluid Mech* 486:161–188
- La Porta A, Voth GA, Crawford AM, Alexander J, Bodenschatz E (2001) Fluid particle accelerations in fully developed turbulence. *Nature* 409:1017–1019
- Lin JC, Rockwell D (2001) Organized oscillations of initially turbulent flow past a cavity. *AIAA J* 39:1139–1151
- Liu X, Katz J (2003) Measurements of pressure distribution by integrating the material acceleration. In: *Cav03-GS-14-001, Fifth international symposium on cavitation (CAV2003)*, Osaka, Japan, 1–4 November, 2003
- Liu X, Katz J (2004) Measurements of pressure distribution in a cavity flow by integrating the material acceleration. In: *HT-FED2004-56373, 2004 ASME heat transfer/fluids engineering summer conference*, Charlotte, NC, USA, 11–15 July, 2004
- Liu X, Thomas FO (2004) Measurement of the turbulent kinetic energy budget of a planar wake flow in pressure gradients. *Exp Fluids* 37:469–482
- O'Hern TJ (1990) An experimental investigation of turbulent shear flow cavitation. *J Fluid Mech* 215:365–391
- Ooi KK, Acosta AJ (1983) The utilization of specially tailored air bubbles as static pressure sensors in a jet. *J Fluids Eng* 106:459–465
- Ott S, Mann J (2000) An experimental investigation of the relative diffusion of particle pairs in three-dimensional turbulent flow. *J Fluid Mech* 422:207–223
- Pope SB (2000) *Turbulent flows*. Cambridge University press, Cambridge
- Press WH, Teukolsky SA, Vetterling WT, Flannery BP (2002) *Numerical recipes in C/C++*. The Press Syndicate of the University of Cambridge, Cambridge
- Ran B, Katz J (1994) Pressure fluctuations and their effect on cavitation inception within water jets. *J Fluid Mech* 262:223–263
- Rockwell D, Knisely C (1979) The organized nature of flow impingement upon a corner. *J Fluids Mech* 93:413–432
- Roth GI (1998) *Developments in particle image velocimetry (PIV) and their application to the measurement of the flow structure and turbulence within a ship bow wave*. PhD dissertation, Johns Hopkins University
- Roth GI, Katz J (2001) Five techniques for increasing the speed and accuracy of PIV interrogation. *Meas Sci Technol* 12:238–245

- Southwell WH (1980) Wave-front estimation from wave-front slope measurements. *J Opt Soc Am* 70:998–1006
- Sridhar G, Katz J (1995) Drag and lift forces on microscopic bubbles entrained by a vortex. *Phys Fluids* 7:389–399
- Tang YP, Rockwell D (1983) Instantaneous pressure fields at a corner associated with vortex impingement. *J Fluid Mech* 126:187–204
- Unal MF, Lin JC, Rockwell D (1997) Force prediction by PIV imaging: a momentum-based approach. *J Fluids Struct* 11:965–971
- Vedula P, Yeung PK (1999) Similarity scaling of acceleration and pressure statistics in numerical simulations of isotropic turbulence. *Phys Fluids* 11:1208–1220
- Voth GA, Satyanarayan K, Bodenschatz E (1998) Lagrangian acceleration measurements at large Reynolds numbers. *Phys Fluids* 10:2268–2280
- Wynanski I, Fiedler H (1969) Some measurements in the self-preserving jet. *J Fluid Mech* 38:577–612
- Yeung PK (2001) Lagrangian characteristics of turbulence and scalar transport in direct numerical simulations. *J Fluid Mech* 427:241–274
- Yeung PK (2002) Lagrangian investigations of turbulence. *Annu Rev Fluid Mech* 34:115–142